

A linear correlation of *p*-band center with the performance of electrochemical CO₂ reduction revealed by Sn single-atom catalysts

Jiangyi Guo, Fengshou Yu*, Yang You, Jiayu Zhan, Lu-Hua Zhang*

National-Local Joint Engineering Laboratory for Energy Conservation in Chemical Process Integration and Resources Utilization, School of Chemical Engineering and Technology, Hebei University of Technology, Tianjin 300130, PR China



ARTICLE INFO

Keywords:

Electrochemical CO₂ reduction
Single-atom catalyst
Coordination environment regulation
p-Orbital energy level
Structure-activity relationships

ABSTRACT

The correlation between *p*-orbital energy level and catalytic activity of electrochemical CO₂ reduction reaction (ECRR) is rarely reported, but significantly desired for further design of highly effective main group single-atom catalysts (SACs). Herein, a series of Sn-SACs (Sn-N₃S₁, Sn-N₃P₁, Sn-N₃B₁, and Sn-N₄) were developed as a model system to explore structure-activity relationships of main group SACs for ECRR. Coordination environment regulation could upshift the *p*-band center of Sn, facilitating the adsorption of intermediates and improving the catalytic activity. Sn-N₃S₁ with the most positive *p*-band center shows a 100 % Faradaic efficiency of CO (FE_{CO}), superior over that of Sn-N₄ and other reported SACs. Notably, the catalytic performance of Sn-SACs shows a linear relationship with *p*-band center of Sn, indicating a high applicability of *p*-band center as a descriptor for catalytic performance. This work provides a new way to boost ECRR by lowering the *p*-orbital energy level of main group metal.

1. Introduction

Electrochemical CO₂ reduction reaction (ECRR) is an enabling strategy for carbon neutral by converting CO₂ into value-added products using renewable electricity [1]. However, the multiple proton-coupled electron transfer (PECT) process for ECRR and competing hydrogen evolution reaction (HER) in aqueous electrolytes result in the large catalytic overpotentials and low Faraday selectivity. The construction of the electrocatalysts with highly-effective active sites is the key for controlling the ECRR pathway and enhancing the catalytic performance [2–4].

The performance of ECRR is regulated by the interaction behavior between active site and intermediate, which is considered to be the coupling between the lowest unoccupied molecular orbital (LUMO) of the intermediate and the highest occupied molecular orbital (HOMO) of the active site. Electronic states regulation has been a promising strategy for facilitating the interaction of active site and the intermediates for numerous reactions [5–8]. For example, we have demonstrated a facile strategy by introducing light element boron to Cu nanoparticles, through which the electronic state of Cu was regulated and therefore the binding strength for reaction intermediate was enhanced [9]. While the complex structure and coordination environment of active sites for

nano-catalyst make the exploration of structure-activity relationships challenging.

Single-atom catalysts (SACs), such as, single metal atoms anchored on the carbon supports, recently have shown the promising activity and selectivity towards ECRR due to the utmost atomic utilization efficiency and distinct local structure [10]. Especially, the fascination of SACs coming from the strong metal-support interaction endows single metal atom with tunable electronic states, thereby resulting in controllable active site-intermediates interaction and thus promoting catalytic properties [11–13]. Previous exploration projects had focused on the 3d transition metals SACs, and decreasing the *d*-orbital energy level of the metal sites in M-N-C usually results in relatively strong adsorption for intermediate e.g. *COOH and thus improved activity and selectivity for ECRR [14–18]. In contrast to 3d transition metals, the main group *p*-block metals have their *d* orbitals in a fully filled state. Nevertheless, the *p*-orbitals of the main group metals are partially filled and expected to confer electrocatalytic activity to the site [19–21]. Although various *p*-block metals SACs have been reported, pinpointing the exact *p*-orbital energy level and further uncovering the specific relationship between electronic structure and catalytic activity of the main group SACs are rarely reported [22–25]. To enable the application of *p*-orbital energy level as a descriptor for ECRR activity, a universal synthesis strategy for

* Corresponding authors.

E-mail addresses: yfsh@hebut.edu.cn (F. Yu), luhuazhang@hebut.edu.cn (L.-H. Zhang).

p-block metals SACs, through which the electronic structure of center metal can be easily and exactly tuned, is strongly desired.

In this regard, a series of Sn-SACs with well-defined coordination environment (Sn-N₃S₁, Sn-N₃P₁, Sn-N₃B₁, and Sn-N₄) were developed as a model system to explore structure-activity relationships of main group SACs for ECRR. The introduction of a secondary heteroatom coordination could upshift the *p*-band center of Sn, therefore facilitating the adsorption of intermediates and improving the catalytic activity. Notably, the catalytic activity of these Sn-SACs shows a linear relationship with *p*-band center of Sn, indicating a highly applicability of *p*-band center as descriptor for ECRR activity. The as-prepared Sn-N₃S₁ with the most positive *p*-band center shows a 100 % Faradaic efficiency of CO (FE_{CO}) at -0.5 V vs. RHE, superior over that of Sn-N₄ (FE_{CO} of 81.3 % at -0.6 V) and other reported SACs. This work provides a new way to boost ECRR by lowering the *p*-orbital energy level of main group metal.

2. Experimental

2.1. Synthesis of catalysts

Synthesis of Sn-N₄: 24 mmol 2-MeIM dissolved in 30 mL of anhydrous methanol and 6 mmol Zn(NO₃)₂·6 H₂O dissolved in 120 mL of anhydrous methanol were mixed. Then 10 mL of DMF solution with 0.1 mmol SnPc was added to the above mixture. The mixed solution was stirred at room temperature for 18 h. The formed powder was filtered and washed three times alternately with DMF and anhydrous methanol, and dried at 60 °C in the vacuum oven. The powder obtained from the above steps was carbonized at 1000 °C for 3 h under Ar to obtain Sn-N₄. N-doped carbon framework (NC) was synthesized without addition of SnPc.

Synthesis of Sn-N₃S₁: The mixture of Sn-N₄ and sulphur powder (molar ratio, 5:1) was dispersed in 20 mL of the mixed solution of carbon tetrachloride and anhydrous ethanol (molar ratio, 4:1), and heated and stirred at 60 °C until dry. The powder was carbonized at 450 °C for 2 h under Ar, then heated to 700 °C (5 °C min⁻¹) and maintained for 2 h. The Sn-N₃S₁ was finally obtained by washing the powder obtained from the above steps with hydrochloric acid (1 M) solution for 12 h at 80 °C to remove clusters and/or nanoparticles. The Sn-N₃P₁ and Sn-N₃B₁ were obtained by a similar procedure except to with triphenylphosphine and boric acid as P and B resources, respectively.

Synthesis of NSC: The mixture of NC and sulphur powder (molar ratio, 5:1) was dispersed in 20 mL of the mixed solution of carbon tetrachloride and anhydrous ethanol (molar ratio, 4:1), heated and stirred at 60 °C until dry. The powder was carbonized at 450 °C for 2 h under Ar, then heated to 700 °C (5 °C min⁻¹) and maintained for 2 h to obtain N, S co-doped carbon framework (NSC). The N, P co-doped carbon framework (NPC) and N, B co-doped carbon framework (NBC) were obtained by a similar procedure except to with triphenylphosphine and boric acid as P and B resources, respectively.

2.2. Electrochemical measurements

All electrochemical measurements in this work were performed using CHI760E electrochemical workstation, in which a conventional three-electrode cell (H-type electrolytic cell) was adopted for ECRR and partitioned by the Nafion membrane. The catalyst ink contained 4.00 mg of sample, 475 μL of ethanol, 475 μL of ultrapure water and 50 μL of Nafion solution (5 wt%), and sonicated for 30 min. A commercial hydrophilic carbon paper with a size of 1 × 1 cm² and dripped with 100 μL of ink was used as the working electrode. Ag/AgCl and platinum wire electrodes were used as the reference and counter electrodes, respectively. All measured potentials were converted to the RHE by the followed equation:

$$E(\text{vs.RHE}) = E(\text{vs.Ag/AgCl}) + 0.224V + 0.0596 \times \text{pH}$$

2.3. DFT calculations

The Vienna Ab initio Simulation Package (VASP) was adopted for the density functional theory (DFT) calculations in this work. The exchange-correlation energy under the generalized gradient approximation (GGA) with norm-conserving pseudopotentials and Perdew–Burke–Ernzerhof (PBE) was adopted to describe the electron–electron interaction. The structure of the sample was built by a single-layer graphene-based system with a sufficiently large vacuum of 15 Å. The convergence criteria for electronic structure and geometry optimization are 1.0 × 10⁻⁵ eV and -0.02 eV/Å, respectively. Planar wave cut-off energy (ENCUT) was set to 400 eV, graphene substrate, using a 3 × 3 × 1 super cell containing atoms. The k-space integral uses a 4 × 4 × 1 Monkhorst-Pack k-point mesh. The ΔG of ECRR steps were calculated by:

$$\Delta G = \Delta E_{\text{DFT}} + \Delta E_{\text{ZPE}} - T\Delta S$$

Where ΔE_{DFT}, ΔE_{ZPE}, and ΔS are the energy from DFT optimization, correction of zero-point energy, and the variation of entropy, respectively. T is the temperature (T = 298.15 K).

The *p*-band center was calculated considering both the unoccupied and occupied orbitals according to the followed equation :

$$\epsilon_p = \frac{\int_{-\infty}^{+\infty} E \times \rho_p dE}{\int_{-\infty}^{+\infty} \rho_p dE}$$

Where ρ_p is the density of *p*-state projected onto Sn nodes.

3. Results and discussion

Density functional theory (DFT) calculations were firstly performed to check the effect of coordination environment on the electronic states of centre Sn atom. With various secondary coordination heteroatoms substitution, the configuration of Sn-N₃S₁, Sn-N₃P₁ and Sn-N₃B₁ were modelled, together with Sn-N₄ for comparison (Fig. 1a). The charge density difference contour shows that Sn-N₄ has a symmetrical charge distribution. With the introduction of S, P and B, a significant charge redistribution can be observed, indicating a strong interaction between the doped heteroatom and the metal sites [26]. Compared to Sn-N₄ (-1.158 eV), the charge density of the Sn center increases after the introduction of S (-1.146 eV), P (-1.003 eV), B (-0.933 eV), which is beneficial for the donation of electrons to the substrates and intermediates in the catalytic reduction reaction (Fig. 1b and S1). The potential interaction promotes us to analyze the *p*-orbital energy level of centre Sn atoms, considering the fact that their *d* orbitals in a fully filled state.

The *p*-orbitals energy level information of the single Sn site was obtained by performing the projected density of states (PDOS) analysis. The *p*-band centers of single Sn atoms in Sn-N₃S₁ (ε_p = -0.369 eV, ε_p is the *p*-band center of the individual Sn site), Sn-N₃P₁ (ε_p = -0.572 eV) and Sn-N₃B₁ (ε_p = -0.803 eV) are approached the Fermi level compared to the original Sn-N₄ (ε_p = -0.922 eV) (Fig. 1c). The upshift of the *p*-band center can lead to more of the adsorbed intermediate's antibonding state pulled above the Fermi level, exhibiting a relatively excellent adsorption of the intermediate [13,27]. In order to validate this speculation, the adsorption state of the *CO₂ on single Sn site was evaluated. As shown in Fig. 1d, the Sn-C bond of Sn-N₃S₁ (2.640 Å) is the shortest, compared to Sn-N₃P₁ (2.668 Å), Sn-N₃B₁ (2.831 Å) and Sn-N₄ (2.872 Å). The result is consistent with the catalytic theory that upshift of the *p*-band center favors the adsorption of *CO₂. The predictions from DFT calculations drive us to synthesize the SACs with the tunable coordination environment and explore their catalytic performance for ECRR.

Sn-N₃S₁, Sn-N₃P₁, Sn-N₃B₁, and Sn-N₄ electrocatalysts were synthesized via a universal two-step pyrolysis strategy. In specific, Sn-N₄ was firstly synthesized by pyrolysis of ZIF-8 precursor containing phthalocyanine (SnPc) molecule as Sn source. Subsequently, a secondary

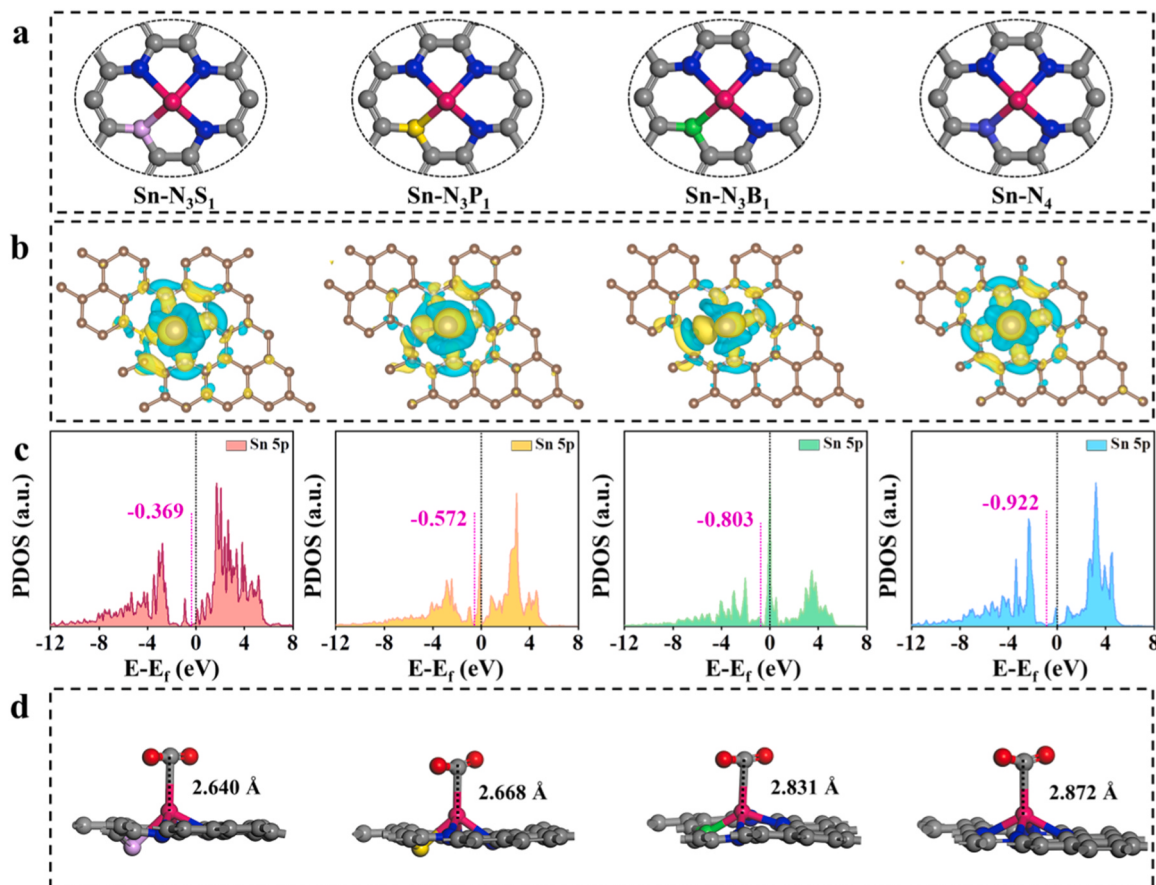


Fig. 1. (a) Structure models, (b) the charge density differences in top views, and (c) the projected density of states (PDOS) of $\text{Sn-N}_3\text{S}_1$, $\text{Sn-N}_3\text{P}_1$, $\text{Sn-N}_3\text{B}_1$, and Sn-N_4 models. The Fermi level is set to 0 eV. (d) The Sn-C bond length with $^*\text{CO}_2$ adsorbed on the above Sn-SAC models. Note: black atom: C, blue atom: N, pink atom: S, yellow atom: P, green atom: B, red atom: Sn. Cyan and yellow represent the decrease and increase in electron density, respectively.

heteroatom (S, P, or B) was embedded into the carbon skeleton of Sn-N_4 samples by a secondary pyrolysis of the mixture of Sn-N_4 carbon samples and the secondary heteroatom sources sulphur, triphenylphosphine, or boric acid (Figs. S2–S4). The synthesized materials were named $\text{Sn-N}_3\text{S}_1$, $\text{Sn-N}_3\text{P}_1$, and $\text{Sn-N}_3\text{B}_1$, respectively.

Scanning electron microscopy (SEM) and transmission electron microscopy (TEM) images indicate the prepared four materials maintain the dodecahedral morphology of ZIF-8 after pyrolysis, and no obvious metal clusters are observed (Fig. 2a–c and S5). Meanwhile, no diffraction peaks associated with crystalline Sn were detected according to X-ray diffraction (XRD) results (Fig. S6), further indicating the absence of aggregated Sn atoms the four samples. Energy-dispersive X-ray spectroscopy (EDS) mappings also reveal that all the elements are homogeneously dispersed throughout the carbon matrix (Fig. 2d–f and S7a). To further explore the dispersion of the Sn species, the aberration-corrected high-angle annular dark-field scanning TEM (AC HAADF-STEM) was carried out. The observed bright spots are recognized as well dispersed Sn atoms (Fig. 2g–i and S7b). The above analysis suggests the successful formation of single-Sn-atom catalysts. In addition, the content of elemental Sn in Sn-N_4 , $\text{Sn-N}_3\text{S}_1$, $\text{Sn-N}_3\text{P}_1$ and $\text{Sn-N}_3\text{B}_1$ are 0.81 wt%, 0.75 wt%, 0.71 wt%, and 0.77 wt%, respectively, revealed by inductively coupled plasma atomic emission spectrometry (ICP-MS).

The chemical composition and elemental states of all the four samples were first evaluated by X-ray photoelectron spectroscopy (XPS, Table S1). The successful doping of S, P and B atoms into carbon skeleton are demonstrated by the formation of C-S (285.5 eV) [28], C-P (285.4 eV) [29], and C-B (284.0 eV) [30] peaks in the high-resolution C 1 s spectra of $\text{Sn-N}_3\text{S}_1$, $\text{Sn-N}_3\text{P}_1$ and $\text{Sn-N}_3\text{B}_1$ samples (Fig. S8). For N 1 s spectra, obvious Sn-N peaks at 399.0 eV are observed for the four

samples (Fig. 3a and S9, Table S2), indicating the coordination of single atom Sn with N [31]. Notably, the characteristic peak at 162.7 eV is considered to the Sn-S bond in S 2p spectrum of $\text{Sn-N}_3\text{S}_1$ sample (Fig. 3b), corroborating the existence of Sn-S coordination [32]. Similarly, Sn-P (129.8 eV) [33] and Sn-B (191.0 eV) [34] coordination are also observed in $\text{Sn-N}_3\text{P}_1$ and $\text{Sn-N}_3\text{B}_1$ samples (Fig. 3c and d). The Sn 3d spectra of the four samples shows two apparent peaks, corresponding to $\text{Sn 3d}_{3/2}$ and $\text{Sn 3d}_{5/2}$ peaks (Fig. 3e). The $\text{Sn 3d}_{5/2}$ peak for the four samples is higher than that for Sn^0 (484.5–485.5 eV) and lower than that for Sn^{4+} (486.3–487.3 eV), indicating the valence of Sn is between 0 and +4. Significantly, the $\text{Sn 3d}_{5/2}$ of $\text{Sn-N}_3\text{S}_1$, $\text{Sn-N}_3\text{P}_1$ and $\text{Sn-N}_3\text{B}_1$ are all shifted to lower binding energies compared with that of Sn-N_4 sample, indicating the enrich electron density of Sn atom in $\text{Sn-N}_3\text{S}_1$, $\text{Sn-N}_3\text{P}_1$ and $\text{Sn-N}_3\text{B}_1$ samples.

The electronic structure and coordination environment of Sn atom in $\text{Sn-N}_3\text{S}_1$, $\text{Sn-N}_3\text{P}_1$ and $\text{Sn-N}_3\text{B}_1$ were further characterized by synchrotron radiation-based X-ray absorption fine structure (XAFS, consisted of X-ray absorption near-edge structure (XANES) and extended X-ray absorption fine structure (EXAFS)). From the XANES data (Fig. 3f), the near-edge lines of $\text{Sn-N}_3\text{S}_1$, $\text{Sn-N}_3\text{P}_1$, and $\text{Sn-N}_3\text{B}_1$ are between Sn foil and SnO , inferring that the oxidation state of Sn atom is located between 0 and +2 in the three samples. For the Fourier transform (FT) EXAFS (FT-EXAFS) analysis, the Sn-Sn bond at 2.79 Å can not be detected for the three samples, further verifying the single atom dispersion manner of all the Sn atoms in Sn-SACs. The FT-EXAFS curve for $\text{Sn-N}_3\text{S}_1$ displays two peaks at 1.63 Å and 2.30 Å (Fig. 3g), corresponding to the Sn-N bond and Sn-S bond, respectively. The $\text{Sn-N}_3\text{P}_1$ sample exhibits an obvious peak at 1.69 Å attributed to the Sn-N/P coordination, and the dominated peak positively shifts 0.06 Å compared to Sn-N bond of Sn-N_4 .

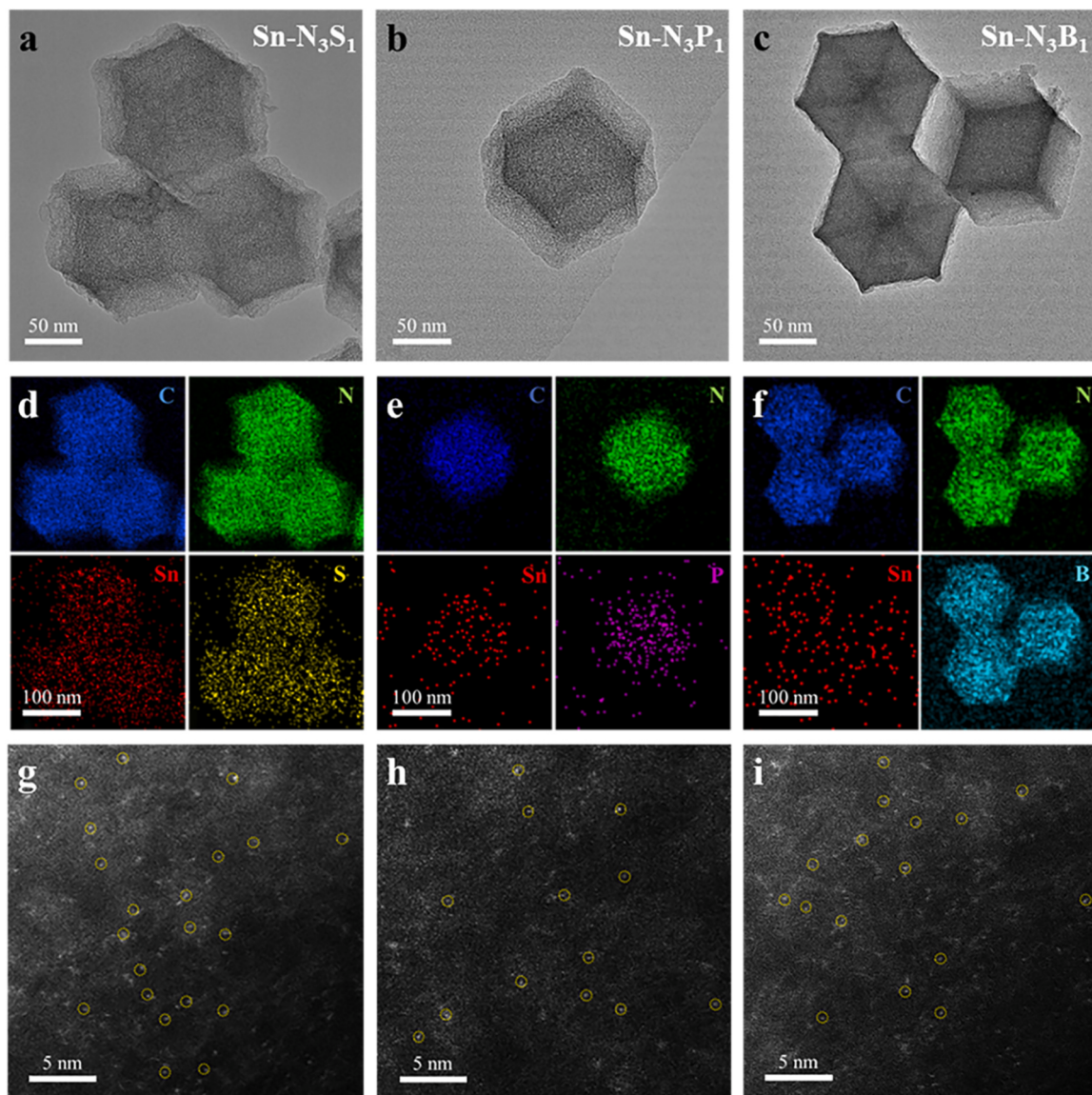


Fig. 2. TEM images of (a) Sn-N₃S₁, (b) Sn-N₃P₁ and (c) Sn-N₃B₁. The corresponding EDS elemental mappings of (d) Sn-N₃S₁, (e) Sn-N₃P₁ and (f) Sn-N₃B₁. AC HAADF-STEM images of (g) Sn-N₃S₁, (h) Sn-N₃P₁ and (i) Sn-N₃B₁.

due to the potential contribution of Sn-P bond (Fig. 3h) [35]. Similarly, for Sn-N₃B₁ sample, one dominant peak at 1.60 Å corresponds to Sn-N/B bond, which shows negatively shift by 0.03 Å compared to Sn-N bond of Sn-N₄ due to the Sn-B bond (Fig. 3i) [36]. Moreover, Sn-N₃S₁ sample can be fitted well for the first coordination shell of Sn with Sn-N and Sn-S, and exhibits four-coordination with three N and one S (Fig. S10 and Table S3). Similarly, Sn-N₃P₁ sample fits well with three N and one P (Fig. S11), and Sn-N₃B₁ model is also obtained (Fig. S12). The wavelet transform (WT) maximum of the Sn-N₃S₁, Sn-N₃P₁, and Sn-N₃B₁ can be attributed to Sn-N/S, Sn-N/P, and Sn-N/B, respectively (Fig. S13). No obvious Sn-Sn bond signals were found by comparing to the WT plots for Sn foil, SnO and SnO₂.

To evaluate the ECRR catalytic performance of the as-prepared Sn-SAC samples, linear sweep voltammetry (LSV) analysis was first conducted in CO₂- or Ar-saturated 0.1 M KHCO₃ solution in H-cell. In comparison with Ar-saturated electrolyte, the four samples exhibit a sharp increase of current density from -0.5 V vs. RHE in CO₂-saturated electrolyte, indicating their excellent performances for ECRR (Fig. S14). Meanwhile, Sn-N₃S₁ shows significantly higher catalytic current than the Sn-N₃P₁, Sn-N₃B₁ and Sn-N₄ samples (Fig. 4a). For example, the

current density of Sn-N₃S₁ can reach 13.81 mA cm⁻² at -1.1 V, higher than those of Sn-N₃P₁ (9.62 mA cm⁻²), Sn-N₃B₁ (7.48 mA cm⁻²) and Sn-N₄ (5.77 mA cm⁻²). To evaluate the Sn-SACs catalytic selectivity, the Faraday efficiency (FE) was evaluated by regulated potential electrolysis. Gaseous and liquid products were quantified by gas chromatography and ¹H nuclear magnetic resonance, respectively. The productions were mainly CO and H₂, while no liquid products were detected for the as-prepared catalysts (Figs. S15–16). For Sn-N₃S₁, the FE_{CO} reaches a maximum of 100 % at -0.5 V, and a high selectivity over 90 % can be achieved from -0.4 to -0.7 V. Sn-N₃P₁ and Sn-N₃B₁ show maximum FE_{CO} of 95.5 % and 92.7 % at -0.6 V. In a sharp contrast, Sn-N₄ shows a low FE_{CO} of 81.3 % at -0.6 V and the CO partial current was decreased to less than 50 % of Sn-N₃S₁ at the measured potential range (Fig. 4b and c). The ECRR catalytic performance for high FE_{CO} of Sn-N₃S₁ sample is superior over the advanced SACs for CO₂ to CO in the H-type cell (Table S4) [37–40]. Based on the number of single Sn atom in Sn-N₃S₁ sample, the maximum TOF for the conversion of CO₂ to CO was calculated to be 3233 h⁻¹, which is more than 3.8 times larger than that of Sn-N₄ (841 h⁻¹) under the same conditions. The kinetics of the conversion of CO₂ to CO was investigated by Tafel plot (Fig. S17). The Tafel

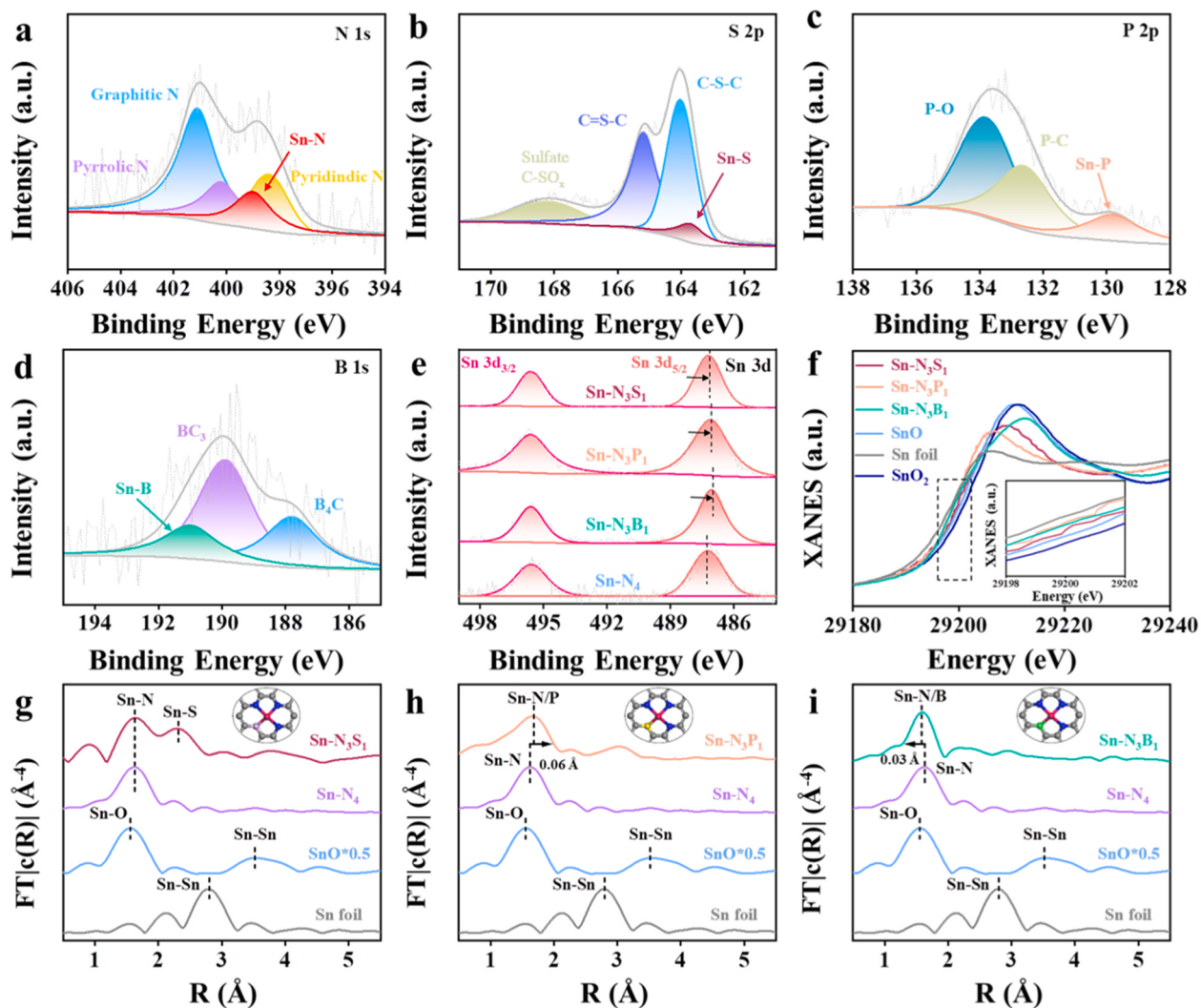


Fig. 3. N 1 s (a) and S 2p (b) XPS spectra for Sn-N₃S₁. P 2p (c) XPS spectra for Sn-N₃P₁ and B 1 s (d) XPS spectra for Sn-N₃B₁. Sn 3d (e) XPS spectra for Sn-N₄, Sn-N₃S₁, Sn-N₃P₁ and Sn-N₃B₁. (f) Sn K-edge XANES spectra of Sn-N₃S₁, Sn-N₃P₁ and Sn-N₃B₁. (g-i) FT k^3 -weighted Sn K-edge EXAFS spectra of Sn-N₃S₁, Sn-N₃P₁, Sn-N₃B₁ and the references.

slope for Sn-N₃S₁ is 128 mV dec⁻¹, which is smaller than those for Sn-N₃P₁ (137 mV dec⁻¹), Sn-N₃B₁ (140 mV dec⁻¹) and Sn-N₄ (176 mV dec⁻¹), indicating the enhanced reaction kinetics for ECRR on Sn-N₃S₁. To further investigate the intrinsic properties, the current was calculated through the normalization by the electrochemical active surface area (ECSA) (Figs. S18–19). The Sn-N₃S₁ catalyst also exhibits a relatively higher ECSA normalized catalytic current than the other samples. On the stability testing, Sn-N₃S₁ exhibits a good stability at -0.5 V in CO₂-saturated 0.1 M KHCO₃ aqueous solution with FE_{CO} > 90% (Fig. S20). The catalyst structure was characterized by XRD patterns, HAADF-STEM and XPS. Based on XRD and HAADF-STEM, the Sn species on Sn-N₃S₁ remains atomically dispersed. From the XPS analysis, the Sn-N and Sn-S bonds were observed. Therefore, Sn is still in the atomic-level dispersion state after reaction (Figs. S21–23). For comparison, the heteroatom doped carbon materials NC, NSC, NPC and NBC in the absence of Sn were also synthesized for reference (Figs. S24–26). These materials show much lower activity than the corresponding Sn-based SACs, proving that atomically dispersed Sn is the real active center of ECRR (Fig. S27).

The impressive activity and selectivity with the various coordination environment of the prepared Sn-SACs sample encourage us to further explore the structure-activity relationships. Throughout the measured potential range, Sn-N₃S₁ shows a relatively larger ECSA normalized CO partial current density (j_{CO} ECSA) than other samples. Taking -0.5 V as

an example, Sn-N₃S₁ exhibits a j_{CO} ECSA of -0.33 mA cm⁻², significantly higher than those of Sn-N₃P₁ (-0.25 mA cm⁻²), Sn-N₃B₁ (-0.24 mA cm⁻²), and Sn-N₄ (-0.18 mA cm⁻²). Notably, a linear relationship is clearly observed by plotting these j_{CO} ECSA vs. p -band centers of the corresponding Sn-SACs (Fig. 4d), indicating that the upshifting of p -band center leads to an enhanced ECRR activity. Meanwhile, the catalytic activity of the four Sn-SACs also reveals a positive linear relationship with the adsorption energy of *CO₂ (Fig. 4e). More interestingly, there is a proportional relationship between the p -band center and E_{ads} of *CO₂, indicating that the upshifting of p -band center promotes adsorption of intermediates (Fig. S28). Those are consistent with above DFT calculation results in Figs. 1c and d that the upshifted p -band center induces the increased adsorption capacity to key intermediates, facilitating the catalytic performance for ECRR. In addition, the effect of p -band center on the kinetic perspective of CO₂ to CO was carried out by TOF analysis. As shown in Fig. 4f, the calculated TOF of the four Sn-SACs for ECRR tends to increase with the upshifting of p -band center, illustrating a kinetics enhancement behavior.

In order to explore the possible reaction pathway and gain an insight into the mechanism of ECRR, we performed electrochemical *in situ* Raman analysis (Fig. 5a). The distinct peaks were assigned to *COO, the C-O stretching and OCO symmetrical stretching of *COOH, respectively [41]. As the voltage increases, these three peaks become more

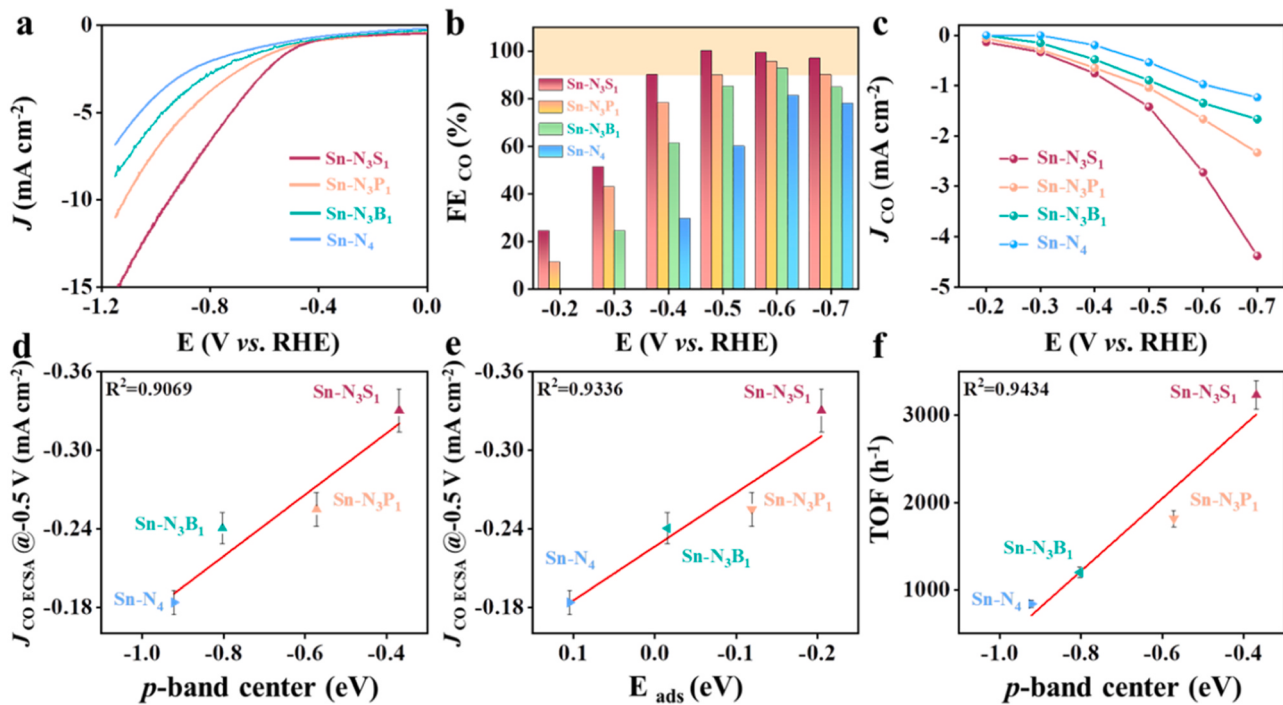


Fig. 4. (a) Linear sweep voltammetry (LSV), (b) FE, and (c) CO partial current density of Sn-N₃S₁, Sn-N₃P₁, Sn-N₃B₁ and Sn-N₄ samples in CO₂-saturated 0.1 M KHCO₃ solution. (d) The dependence of ECSA normalized CO partial current density at -0.5 V with the *p*-band center and (e) E_{ads} of *CO₂ on active single Sn site. (f) Linear plot of the calculated TOF for ECRR to CO at -0.7 V vs. *p*-band center of the corresponding Sn-SACs.

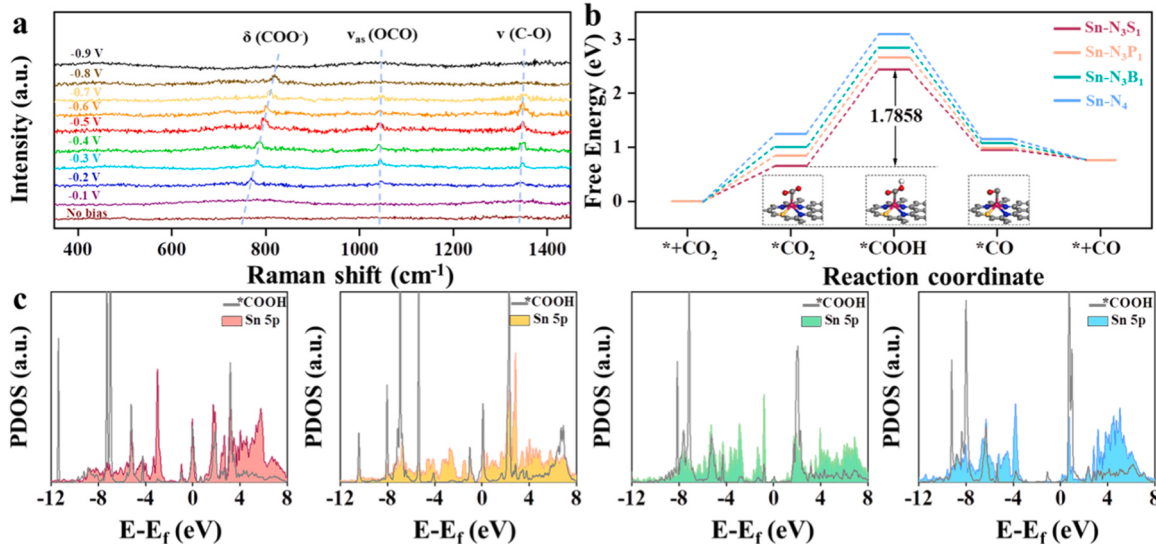


Fig. 5. (a) *In situ* Raman spectra of ECRR at the Sn-N₃S₁ surface in 0.1 M CO₂-saturated KHCO₃. (b) Gibbs free energy diagrams of ECRR on Sn-N₃S₁, Sn-N₃P₁, Sn-N₃B₁, and Sn-N₄ sites. (c) PDOS of the C 2p of *COOH and the Sn 5p of Sn-N₃S₁, Sn-N₃P₁, Sn-N₃B₁, and Sn-N₄ models.

significant and reach a maximum at -0.5 V. When voltages higher than -0.5 V were applied, the three peaks decreased significantly due to rapid depletion of the intermediates. Moreover, the redshift of vibrational frequency for intermediate with the potential becomes more negative results from the change in the electric field around the surface [42].

Additionally, the DFT calculations were subsequently utilized to unveil the catalytic reaction mechanism of Sn-N₃S₁, Sn-N₃P₁, Sn-N₃B₁ and Sn-N₄ for ECRR (Fig. S29). Based on DFT calculations, the formation of *COOH intermediate was the rate-determining step (RDS) as a result of the relatively larger free energy for Sn-N₄ (Fig. 5b and Table S5). For

the asymmetric structures, the free energy for the *COOH intermediate formation decreases significantly, which was attributed to the upshifting of *p*-band center of Sn after the heteroatoms of S, P or B replacement. In specific, the introduction of the Sn-S coordination greatly decreased the free energy for the intermediate of *COOH formation from 1.8445 eV (Sn-N₄) to 1.7858 eV. Moreover, there are more overlaps of the electronic states between the C 2p orbitals of *COOH and the 5p orbitals of Sn atom on the Sn-N₃S₁ site than those on the Sn-N₄ site, further supporting the stronger binding of *COOH on the Sn-N₃S₁ site (Fig. 5c). Besides, to further clarify the electronic band structure between active sites and adsorbed *COOH, we analyze the PDOS among the C 2p of

*COOH and the Sn 5p of Sn-N₃S₁, Sn-N₃P₁, Sn-N₃B₁, and Sn-N₄ (2–5p orbital hybridization). More overlapping peaks between Sn 5p orbitals and C 2p orbitals around the Fermi level appear in the PDOS of Sn-N₃S₁, reflecting the much stronger hybridisation between the Sn single atoms and the C atoms of *COOH in Sn-N₃S₁ than in other catalysts. Accordingly, the strong orbital hybridisation effectively form the chemical bonds of Sn-C and then promote the electrons transfer from Sn single atom to *COOH. To quantitatively analyze the overlapping degree ($P_{\text{Sn}-\text{*COOH}}$), an equation of $P_{\text{Sn}-\text{*COOH}} = A_{\text{Overlap}} / A_{\text{C } 2\text{p}}$ was defined, where A_{Overlap} and $A_{\text{C } 2\text{p}}$ stand for the overlapped region area and the C 2p orbitals, respectively. The $P_{\text{Sn}-\text{*COOH}}$ of Sn-N₃S₁ is 57.8 %, higher than those of Sn-N₃P₁ (56.9 %), Sn-N₃B₁ (56.2 %), and Sn-N₄ (55.1 %). The $P_{\text{Sn}-\text{*COOH}}$ and the free energy for *COOH formation of the four samples are inversely proportional in magnitude. The higher $P_{\text{Sn}-\text{*COOH}}$ for Sn-N₃S₁ implies an easier electron transfer from Sn to *COOH and a stronger stabilization of *COOH [43]. Therefore, the introduction of a secondary heteroatom facilitates the formation of *COOH intermediates and further enhances the catalytic performance. Meanwhile, the competing HER is more energy-demanding on active single Sn site, resulting in less H₂ evolution (Fig. S30 and Table S6). The introduction of secondary heteroatom coordination can tune the p-band center of Sn, thereby enhancing the catalytic activity and changing selectivity.

4. Conclusion

We have demonstrated a universal coordination environment modulation strategy, through which the electronic structure of single atom Sn varies with a secondary heteroatom species. Based on the theoretical analysis, the p-band center of Sn atom was upshifted by introducing the secondary heteroatom coordination, facilitating the adsorption of intermediates and boosting the catalytic performance. The catalytic performance of these Sn-based SACs shows a linear relationship with p-band center of Sn, indicating a highly applicable of p-band center as descriptor for catalytic performance. This work systematically explores the correlation of coordination environment and the catalytic performance, and modulation mechanism of different heteroatoms for catalytic performance enhancement of SACs. These findings together with the universal synthesis method for SACs can be extensively applied to other electrochemical transformation of proton-coupled electron transport.

CRediT authorship contribution statement

Yang You: Writing – original draft. **Jiayu Zhan:** Writing – original draft. **Jiangyi Guo:** Writing – original draft. **Fengshou Yu:** Writing – review & editing. **Lu-Hua Zhang:** Writing – review & editing.

Declaration of Competing Interest

The authors declare that they have no known competing financial interests or personal relationships that could have appeared to influence the work reported in this paper.

Data Availability

The authors do not have permission to share data.

Acknowledgements

This work was supported by the National Natural Science Foundation of China (Nos. 22278108 and 22008048), Natural Science Foundation of Tianjin (22JCYBJC00250), Natural Science Foundation for Outstanding Youth Scholars of Hebei Province (No. B2021202061), Natural Science Foundation of Hebei Province (No. B2021202010), and the State Key Laboratory of Fine Chemicals, Dalian University of Technology (KF2108).

Appendix A. Supporting information

Supplementary data associated with this article can be found in the online version at doi:10.1016/j.apcatb.2024.124160.

References

- [1] X. Tan, C. Yu, Y. Ren, S. Cui, W. Li, J. Qiu, Recent advances in innovative strategies for the CO₂ electroreduction reaction, *Energy Environ. Sci.* 14 (2021) 765–780, <https://doi.org/10.1039/D0EE02981E>.
- [2] K. Zhao, X. Quan, Carbon-based materials for electrochemical reduction of CO₂ to C₂₊ oxygenates: recent progress and remaining challenges, *ACS Catal.* 11 (2021) 2076–2097, <https://doi.org/10.1021/acscatal.0c04714>.
- [3] F. Yu, G. Liu, J. Zhan, Y. Jia, Z. Feng, B. Shen, N.R. Shiju, L.-H. Zhang, Self-driven electron enrichment of ultrafine PdAu nanoparticles for electrochemical CO₂ reduction: high applicability of work function as an activity descriptor, *Appl. Catal. B Environ.* 338 (2023) 122931, <https://doi.org/10.1016/j.apcatb.2023.122931>.
- [4] D. Wang, J. Mao, C. Zhang, J. Zhang, J. Li, Y. Zhang, Y. Zhu, Modulating microenvironments to enhance CO₂ electroreduction performance, *eScience* 3 (2023) 100119, <https://doi.org/10.1016/j.esci.2023.100119>.
- [5] J. Zhu, M. Xiao, D. Ren, R. Gao, X. Liu, Z. Zhang, D. Luo, W. Xing, D. Su, A. Yu, Z. Chen, Quasi-covalently coupled Ni–Cu atomic pair for synergistic electroreduction of CO₂, *J. Am. Chem. Soc.* 144 (2022) 9661–9671, <https://doi.org/10.1021/jacs.2c00937>.
- [6] R. Zhang, Y. Guo, S. Zhang, D. Chen, Y. Zhao, Z. Huang, L. Ma, P. Li, Q. Yang, G. Liang, C. Zhi, Efficient ammonia electrosynthesis and energy conversion through a Zn-nitrate battery by Iron doping engineered nickel phosphide catalyst, *Adv. Energy Mater.* 12 (2022) 2103872, <https://doi.org/10.1002/aenm.202103872>.
- [7] D. Cao, H. Xu, H. Li, C. Feng, J. Zeng, D. Cheng, Volcano-type relationship between oxidation states and catalytic activity of single-atom catalysts towards hydrogen evolution, *Nat. Commun.* 13 (2022) 5843, <https://doi.org/10.1038/s41467-022-33589-y>.
- [8] Y. Dai, H. Li, C. Wang, W. Xue, M. Zhang, D. Zhao, J. Xue, J. Li, L. Luo, C. Liu, X. Li, P. Cui, Q. Jiang, T. Zheng, S. Gu, Y. Zhang, J. Xiao, C. Xia, J. Zeng, Manipulating local coordination of copper single atom catalyst enables efficient CO₂-to-CH₄ conversion, *Nat. Commun.* 14 (2023) 3382, <https://doi.org/10.1038/s41467-023-39048-6>.
- [9] L.-H. Zhang, Y. Jia, J. Zhan, G. Liu, F. Yu, Dopant-induced electronic states regulation boosting electroreduction of dilute nitrate to ammonium, *Angew. Chem. Int. Ed.* 62 (2023) e202303483, <https://doi.org/10.1002/anie.202303483>.
- [10] S. Wang, L. Wang, D. Wang, Y. Li, Recent advances of single-atom catalysts in CO₂ conversion, *Energy Environ. Sci.* 16 (2023) 2759–2773, <https://doi.org/10.1039/D3EE00037K>.
- [11] X. Sun, L. Sun, G. Li, Y. Tu, C. Ye, J. Yang, J. Low, X. Yu, J.H. Bitter, Y. Lei, D. Wang, Y. Li, Phosphorus tailors the d-band center of copper atomic sites for efficient CO₂ photoreduction under visible-Light Irradiation, *Angew. Chem. Int. Ed.* 61 (2022) e202207677, <https://doi.org/10.1002/anie.202207677>.
- [12] F. Yu, J. Zhan, D. Chen, J. Guo, S. Zhang, L.-H. Zhang, Electronic states regulation induced by the synergistic effect of Cu clusters and Cu-S₁N₃ sites boosting electrocatalytic performance, *Adv. Funct. Mater.* 33 (2023) 2214425, <https://doi.org/10.1002/adfm.202214425>.
- [13] J. Yu, J. Li, C.-Y. Xu, Q. Li, Q. Liu, J. Liu, R. Chen, J. Zhu, J. Wang, Modulating the d-band centers by coordination environment regulation of single-atom Ni on porous carbon fibers for overall water splitting, *Nano Energy* 98 (2022) 107266, <https://doi.org/10.1016/j.nanoen.2022.107266>.
- [14] D. Chen, L.H. Zhang, J. Du, H. Wang, J. Guo, J. Zhan, F. Li, F. Yu, A tandem strategy for enhancing electrochemical CO₂ reduction activity of single-atom Cu-S₁N₃ catalysts via integration with Cu nanoclusters, *Angew. Chem. Int. Ed.* 60 (2021) 24022–24027, <https://doi.org/10.1002/anie.202109579>.
- [15] X. Yang, J. Cheng, X. Yang, Y. Xu, W. Sun, N. Liu, J. Zhou, Single Ni active sites with a nitrogen and phosphorus dual coordination for an efficient CO₂ reduction, *Nanoscale* 14 (2022) 6846–6853, <https://doi.org/10.1039/D2NR00294A>.
- [16] B. Mohanty, S. Basu, B.Kumar Jena, Transition metal-based single-atom catalysts (TM-SACs): rising materials for electrochemical CO₂ reduction, *J. Energy Chem.* 70 (2022) 444–471, <https://doi.org/10.1016/j.jechem.2022.02.045>.
- [17] Z. Chen, X. Zhang, W. Liu, M. Jiao, K. Mou, X. Zhang, L. Liu, Amination strategy to boost the CO₂ electroreduction current density of M–N/C single-atom catalysts to the industrial application level, *Energy Environ. Sci.* 14 (2021) 2349–2356, <https://doi.org/10.1039/D0EE04052E>.
- [18] S. Liu, M. Jin, J. Sun, Y. Qin, S. Gao, Y. Chen, S. Zhang, J. Luo, X. Liu, Coordination environment engineering to boost electrocatalytic CO₂ reduction performance by introducing boron into single-Fe-atomic catalyst, *Chem. Eng. J.* 437 (2022) 135294, <https://doi.org/10.1016/j.cej.2022.135294>.
- [19] C. Xiao, W. Song, J. Liang, J. Zhang, Z. Huang, J. Zhang, H. Wang, C. Zhong, J. Ding, W. Hu, P-block tin single atom catalyst for improved electrochemistry in a lithium-sulfur battery: a theoretical and experimental study, *J. Mater. Chem. A* 10 (2022) 3667–3677, <https://doi.org/10.1039/DITA09422J>.
- [20] Y. Deng, J. Zhao, S. Wang, R. Chen, J. Ding, H.-J. Tsai, W.-J. Zeng, S.-F. Hung, W. Xu, J. Wang, F. Jaouen, X. Li, Y. Huang, B. Liu, Operando spectroscopic analysis of axial oxygen-coordinated single-Sn-atom sites for electrochemical CO₂ reduction, *J. Am. Chem. Soc.* 145 (2023) 7242–7251, <https://doi.org/10.1021/jacs.2c12952>.
- [21] D. Fang, L. Zhang, Y. Niu, Y. Wang, Q. Su, J. Wang, C. Wang, Elevating the p-band centre of SnO₂ nanosheets through W incorporation for promoting CO₂

- electroreduction, Dalton Trans. 51 (2022) 541–552, <https://doi.org/10.1039/D1DT03152J>.
- [22] T. Wang, X. Cao, H. Qin, L. Shang, S. Zheng, F. Fang, L. Jiao, P-block atomically dispersed antimony catalyst for highly efficient oxygen reduction reaction, Angew. Chem. Int. Ed. 60 (2021) 21237–21241, <https://doi.org/10.1002/anie.202108599>.
- [23] S. Li, X. Lu, S. Zhao, M. Ceccato, X.-M. Hu, A. Roldan, M. Liu, K. Daasbjerg, P-block indium single-atom catalyst with low-coordinated In–N motif for enhanced electrochemical CO₂ reduction, ACS Catal. 12 (2022) 7386–7395, <https://doi.org/10.1021/acscatal.2c01805>.
- [24] W. Xie, H. Li, G. Cui, J. Li, Y. Song, S. Li, X. Zhang, J.Y. Lee, M. Shao, M. Wei, NiSn atomic pair on an integrated electrode for synergistic electrocatalytic CO₂ reduction, Angew. Chem. Int. Ed. 60 (2021) 7382–7388, <https://doi.org/10.1002/anie.202014655>.
- [25] L. Wang, L. Wang, L. Zhang, H. Liu, J. Yang, Perspective of p-block single-atom catalysts for electrocatalysis, Trends Chem. 4 (2022) 1135–1148, <https://doi.org/10.1016/j.trechn.2022.09.010>.
- [26] C. Wang, K. Wang, Y. Feng, C. Li, X. Zhou, L. Gan, Y. Feng, H. Zhou, B. Zhang, X. Qu, H. Li, J. Li, A. Li, Y. Sun, S. Zhang, G. Yang, Y. Guo, S. Yang, T. Zhou, F. Dong, K. Zheng, L. Wang, J. Huang, Z. Zhang, X. Han, Co and Pt dual-single-atoms with oxygen-coordinated Co-O-Pt dimer sites for ultrahigh photocatalytic hydrogen evolution efficiency, Adv. Mater. 33 (2021) e2003327, <https://doi.org/10.1002/adma.202003327>.
- [27] X. Hu, Y. Liu, W. Cui, X. Yang, J. Li, S. Zheng, B. Yang, Z. Li, X. Sang, Y. Li, L. Lei, Y. Hou, Boosting industrial-level CO₂ electroreduction of N-doped carbon nanofibers with confined tin-nitrogen active sites via accelerating proton transport kinetics, Adv. Funct. Mater. 33 (2022) 2208781, <https://doi.org/10.1002/adfm.202208781>.
- [28] H. Zhang, Q. Sun, Q. He, Y. Zhang, X. He, T. Gan, H. Ji, Single Cu atom dispersed on S,N-codoped nanocarbon derived from shrimp shells for highly-efficient oxygen reduction reaction, Nano Res. 15 (2022) 5995–6000, <https://doi.org/10.1007/s12274-022-4289-3>.
- [29] K. Yuan, D. Lutzenkirchen-Hecht, L. Li, L. Shuai, Y. Li, R. Cao, M. Qiu, X. Zhuang, M.K.H. Leung, Y. Chen, U. Scherf, Boosting oxygen reduction of single iron active sites via geometric and electronic engineering: nitrogen and phosphorus dual coordination, J. Am. Chem. Soc. 142 (2020) 2404–2412, <https://doi.org/10.1021/jacs.9b11852>.
- [30] X. Yu, P. Han, Z. Wei, L. Huang, Z. Gu, S. Peng, J. Ma, G. Zheng, Boron-doped graphene for electrocatalytic N₂ reduction, Joule 2 (2018) 1610–1622, <https://doi.org/10.1016/j.joule.2018.06.007>.
- [31] X. Zu, X. Li, W. Liu, Y. Sun, J. Xu, T. Yao, W. Yan, S. Gao, C. Wang, S. Wei, Y. Xie, Efficient and robust carbon dioxide electroreduction enabled by atomically dispersed Sn^{δ+} sites, Adv. Mater. 31 (2019) e1808135, <https://doi.org/10.1002/adma.201808135>.
- [32] S. Zhao, Y. Qin, T. Guo, S. Li, X. Liu, M. Ou, Y. Wu, Y. Chen, SnS nanoparticles grown on Sn-atom-modified N,S-codoped mesoporous carbon nanosheets as electrocatalysts for CO₂ reduction to formate, ACS Appl. Nano Mater. 4 (2021) 2257–2264, <https://doi.org/10.1021/acsanm.0c03361>.
- [33] W. Fan, Y. Gao, Q. Hui, Z. Ma, H. Gan, X. Xia, H. Liu, A closed-ended MXene armor on hollow Sn₄P₃ nanospheres for ultrahigh-rate and stable sodium storage, Chem. Eng. J. 465 (2023) 142963, <https://doi.org/10.1016/j.cej.2023.142963>.
- [34] Z. Li, T. Zhang, R.M. Yadav, J. Zhang, J. Wu, Boron doping in tin catalysts towards gas-phase CO₂ to formic acid/formate electroreduction with high production efficiency and rate, J. Electrochem. Soc. 167 (2020) 114508, <https://doi.org/10.1149/1945-7111/aba6c6>.
- [35] T. Huang, Y. Sun, J. Wu, Z. Shi, Y. Ding, M. Wang, C. Su, Y.Y. Li, J. Sun, Altering local chemistry of single-atom coordination boosts bidirectional polysulfide conversion of Li–S batteries, Adv. Funct. Mater. 32 (2022) 2203902, <https://doi.org/10.1002/adfm.202203902>.
- [36] Y. Gu, S. Wang, H. Shi, J. Yang, S. Li, H. Zheng, W. Jiang, J. Liu, X. Zhong, J. Wang, Atomic Pt embedded in BNC nanotubes for enhanced electrochemical ozone production via an oxygen intermediate-rich local environment, ACS Catal. 11 (2021) 5438–5451, <https://doi.org/10.1021/acscatal.1c00413>.
- [37] E. Zhang, T. Wang, K. Yu, J. Liu, W. Chen, A. Li, H. Rong, R. Lin, S. Ji, X. Zheng, Y. Wang, L. Zheng, C. Chen, D. Wang, J. Zhang, Y. Li, Bismuth single atoms resulting from transformation of metal-organic frameworks and their use as electrocatalysts for CO₂ reduction, J. Am. Chem. Soc. 141 (2019) 16569–16573, <https://doi.org/10.1021/jacs.9b08259>.
- [38] W. Ni, Y. Gao, Y. Lin, C. Ma, X. Guo, S. Wang, S. Zhang, Nonnitrogen coordination environment steering electrochemical CO₂-to-CO conversion over single-atom tin catalysts in a wide potential window, ACS Catal. 11 (2021) 5212–5221, <https://doi.org/10.1021/acscatal.0c05514>.
- [39] J. Guo, W. Zhang, L.H. Zhang, D. Chen, J. Zhan, X. Wang, N.R. Shiju, F. Yu, Control over electrochemical CO₂ reduction selectivity by coordination engineering of tin single-atom catalysts, Adv. Sci. 8 (2021) e2102884, <https://doi.org/10.1002/advs.202102884>.
- [40] T. Wang, X. Sang, W. Zheng, B. Yang, S. Yao, C. Lei, Z. Li, Q. He, J. Lu, L. Lei, L. Dai, Y. Hou, Gas diffusion strategy for inserting atomic iron sites into graphitized carbon supports for unusually high-efficient CO₂ electroreduction and high-performance Zn-CO₂ batteries, Adv. Mater. 32 (2020) e2002430, <https://doi.org/10.1002/adma.202002430>.
- [41] W. Shan, R. Liu, H. Zhao, Z. He, Y. Lai, S. Li, G. He, J. Liu, In situ surface-enhanced raman spectroscopic evidence on the origin of selectivity in CO₂ electrocatalytic reduction, ACS Nano 14 (2020) 11363–11372, <https://doi.org/10.1021/acsnano.0c03534>.
- [42] Y. Wu, P. Zhai, S. Cao, Z. Li, B. Zhang, Y. Zhang, X. Nie, L. Sun, J. Hou, Beyond d orbits: steering the selectivity of electrochemical CO₂ reduction via hybridized sp band of sulfur-Incorporated porous Cd architectures with dual collaborative sites, Adv. Energy Mater. 10 (2020) 2002499, <https://doi.org/10.1002/aenm.202002499>.
- [43] Y. Qin, G. Zhan, C. Tang, D. Yang, X. Wang, J. Yang, C. Mao, Z. Hao, S. Wang, Y. Qin, H. Li, K. Chen, M. Liu, J. Li, Homogeneous vacancies-enhanced orbital hybridization for selective and efficient CO₂-to-CO electrocatalysis, Nano Lett. 23 (2023) 9227–9234, <https://doi.org/10.1021/acs.nanolett.3c01905>.